ARTICLE

Check for updates

Zero-field skyrmionic states and in-field edge-skyrmions induced by boundary tuning

Jonas Spethmann [1✉], Elena Y. Vedmedenko[1], Roland Wiesendanger [1], André Kubetzka [1] & Kirsten von Bergmann [1]

When magnetic skyrmions are moved via currents, they do not strictly travel along the path of the current, instead their motion also gains a transverse component. This so-called skyrmion Hall effect can be detrimental in potential skyrmion devices because it drives skyrmions towards the edge of their hosting material where they face potential annihilation. Here we experimentally modify a skyrmion model system—an atomic Pd/Fe bilayer on Ir(111)—by decorating the film edge with ferromagnetic Co/Fe patches. Employing spin-polarized scanning tunneling microscopy, we demonstrate that this ferromagnetic rim prevents skyrmion annihilation at the film edge and stabilizes skyrmions and target states in zero field. Furthermore, in an external magnetic field the Co/Fe rim can give rise to skyrmions pinned to the film edge. Spin dynamics simulations reveal how a combination of different attractive and repulsive skyrmion-edge interactions can induce such an edge-pinning effect for skyrmions.

[1] Department of Physics, University of Hamburg, Hamburg, Germany. ✉email: jspethma@physnet.uni-hamburg.de

Magnetic skyrmions are whirling spin textures with topological properties that make them robust against external perturbations. They were first described theoretically[1,2] and later found experimentally in systems with broken structural inversion symmetry such as chiral magnets[3,4] or magnetic ultra-thin films[5,6]. Their well-investigated transport properties[7–11] make them interesting candidates as information carriers in future generation spintronic devices, such as racetrack memories[12,13], logic gates[14–16] or recently proposed applications that exploit Brownian skyrmion motion[17–19]. Skyrmions are typically stabilized in applied magnetic fields by an interplay of exchange interaction, Dzyaloshinskii–Moriya interaction (DMI)[20,21], and perpendicular magnetocrystalline anisotropy (PMA). The size of skyrmions ranges from sub-10 nm in epitaxially grown ultra-thin metal films, in which skyrmions are stable at cryogenic temperatures[5,6,22,23], to room-temperature skyrmions in multilayer films with diameters between 30 nm and 2 µm[24–27].

One limitation that potential skyrmion applications may face is the occurrence of the skyrmion Hall effect (SkHE), which arises due to the topological nature of the skyrmions and drives them towards the edge of their hosting material when they are moved via currents[28–30]. This can cause skyrmion annihilation at the edge[31–33], which would be detrimental to their use in such devices. One proposal to mitigate this problem is to use skyrmionic states with compensated topological charge ($Q = 0$) that theoretically do not show the SkHE, e.g., antiferromagnetic skyrmions[34–36] or 2π skyrmions, which are also called target states[37–41]. Alternatively, it was proposed to manipulate the magnetic properties of the skyrmion material itself by creating a potential well that guides the skyrmion along a desired pathway[32,42,43]. Recently two groups have made experimental advances in this regard using sputter-deposited thin-film systems: one group created skyrmion-stabilizing tracks with weakened PMA and DMI by slightly altering their Pt/Co/MgO film with focused He+ ion beam irradiation[44]. The other group was able to grow a multilayer film patterned with high-PMA areas that repel skyrmions[27].

Here we investigate skyrmion-edge interactions in an epitaxially grown model-type system using spin-polarized scanning tunneling microscopy (SP-STM)[45,46], which employs the tunneling magnetoresistance effect (TMR). Our model system is an atomic Pd/Fe bilayer on the surface of an Ir(111) single crystal, which—at cryogenic temperatures—has a cycloidal spin spiral as its magnetic ground state. Under the application of an external magnetic field, the spin spiral turns first into a skyrmion lattice and then into individual skyrmions with diameters of 2–3 nm[6,47]. Figure 1a shows an SP-STM image of such a Pd/Fe island. The spin spiral can be identified by periodically occurring stripes of a darker and brighter signal. The island shape has a strong effect on the propagation direction of the spin spiral: the spiral stripes are oriented along the shorter island extension and bend in such a way, that they connect perpendicular to the Pd island edge. This configuration is preferred over a parallel alignment to the island edge, because it avoids the formation of a ferromagnetically ordered island rim[48], and in this way allows the DMI energy to be further reduced by edge tilting effects[37,49].

These results show that the island edge has a clear influence onto the details of the magnetic state and the question arises, whether the island edge can be utilized to manipulate the magnetic state inside the Pd/Fe island in a desired fashion. In this work, we tune the properties of the Pd/Fe edge by growing a self-assembled ferromagnetic Co/Fe bilayer adjacent to it. We find that the Co/Fe bilayer has an immediate effect on the spin spiral ground state, stabilizes skyrmions and target states at zero field, and gives rise to skyrmions pinned to the Pd/Fe island edge in

applied magnetic fields. Finally, we perform spin dynamics simulations to investigate the role of different magnetic parameters in causing these edge effects.

Results

Tuning the Pd/Fe island edge. We attempt a tuning of the Pd/Fe island edges by decorating them with a Co/Fe bilayer. For this, approximately 0.2 atomic layers of Co are deposited onto an existing Pd/Fe/Ir(111) sample at room temperature. The Co grows either on the uncovered Ir surface or on top of the Fe monolayer, where it preferentially attaches itself to the Pd island edge (Fig. 1b). In this way free-standing Pd/Fe islands are typically fully surrounded by Co/Fe; only rarely do we observe Co islands on top of Pd/Fe. Figure 1c shows an STM constant-current image of a Pd/Fe island surrounded by Co/Fe at the right and upper edge, while the left island rim is adjacent to a buried Ir(111) step edge.

Note that the Co/Fe areas show regular dislocation lines that originate from a structural reconstruction. This reconstruction is present in three rotational domains due to the hexagonal symmetry of the Ir(111) surface. We find that the Co/Fe bilayer is ferromagnetic, with two contrast levels per rotational domain and up to six different contrast levels in total (Supplementary Fig. S1). We conclude that the easy magnetization axis of Co/Fe
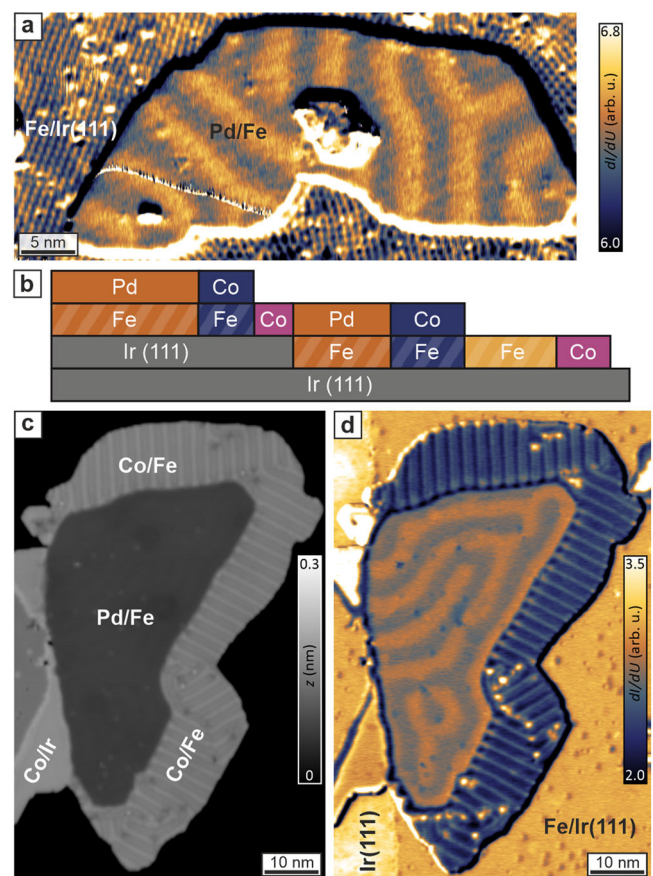

Fig. 1 The Pd/Fe/Ir(111) system with Co/Fe-decorated edges. a differential conductance (dI/dU) map of a Pd/Fe island on Ir(111) showing the spin spiral state (tunneling current $I = 2$ nA, bias voltage $U = 15$ mV). **b** Sketch of the sample composition after Co deposition. **c, d** Constant-current image with apparent sample height z and simultaneously recorded dI/dU map of a Pd/Fe island surrounded by Co/Fe ($I = 2$ nA, $U = -310$ mV); with the Co/Fe rim, the spin spiral stripes are oriented parallel to the island edges.

must be in-plane and from measurements with a known tip magnetization axis, we derive the easy magnetization axis of Co/Fe to be perpendicular to its dislocation lines (Supplementary Fig. S2).

Figure 1d shows a differential conductance (dI/dU) map of the same Pd/Fe island as shown in Fig. 1b. Here the magnetic contrast of the Pd/Fe spin spiral in the magnetic virgin state is observed. Comparison with the island in Fig. 1a demonstrates that the adjacent Co/Fe strongly affects the path of the spin spiral stripes, which are now oriented parallel to the Co/Fe-decorated island edges. Only at the left island edge, which is not next to a Co/Fe area, the spiral stripes seem to prefer an orthogonal orientation. Due to the shape of the island, the spin spiral in the interior of the island is also affected by the Co/Fe edge and is much more disordered when compared to Fig. 1a.

Zero-field skyrmions and target states. In Fig. 2a an overview image with several Pd/Fe islands—each surrounded by Co/Fe—is shown. At the bias voltage chosen here, one can also discriminate between hcp-stacked (orange) and fcc-stacked (yellow) Pd/Fe islands, see inset. These two Pd/Fe stackings exhibit subtle differences in their magnetic interaction parameters which lead to, e.g., a slightly larger spiral period in the case of hcp-stacked Pd/Fe. Note that these images were measured with a non-magnetic tip, utilizing the non-collinear magnetoresistance (NCMR) effect, which is caused by a mixing of spin channels that occurs in non-collinear spin structures and is highly sensitive to fast-rotating spin textures[50]. The contrast originating from the NCMR effect differs from that of the TMR: the spin spirals in Pd/Fe/Ir(111) are inhomogeneous, i.e., due to the PMA of the system the out-of-plane sections are more collinear, while the nearest-neighbor angle in in-plane areas becomes larger. When imaged with NCMR contrast, the tip is therefore equally sensitive to all in-plane sections of the spiral, which effectively halves the measured distance between the dark stripes compared to TMR measurements. As shown in the inset of Fig. 2b, skyrmions can also be detected using the NCMR effect: depending on their size they can appear as dark rings or dots, because again the in-plane sections of a skyrmion are strongly non-collinear while the skyrmion center is mostly collinear below a critical external field[50].

In both Pd/Fe stackings, the Co/Fe-decorated edges appear to affect the spin spirals in a similar fashion: the spin spiral stripes prefer to be parallel to the island edges, which often leads to the formation of more exotic spin structures in the magnetic virgin state of the system (Fig. 2a–d), including skyrmions (white arrows) and target states (black arrows). These zero-field skyrmions are often observed in rather small Pd/Fe islands or corners of larger islands, where the surrounding Co/Fe seemingly prevents the skyrmion from connecting to the island edge. Typically external fields above 1 T are necessary to stabilize skyrmions in Pd/Fe/Ir(111) and target states (see Fig. 2e for the spin structure and expected NCMR contrast) have not been observed in Pd/Fe/Ir(111) prior to this publication, despite an effort to stabilize them in confined geometries[41]. However, in samples with added Co/Fe at the boundaries, they appear frequently in zero field. Depending on the Pd/Fe island size and geometry, the target states often deviate from their ideal circular shape and their diameter may vary in the range of 10–20 nm. The target state shown in Fig. 2c is surrounded by an almost complete third ring, which would make it a 3π skyrmion, were it not for the small section that is connected to the island rim. Nevertheless, these findings suggest that it may be possible to stabilize and study $k\pi$ skyrmions with $k > 2$ by carefully adjusting the size and shape of the Pd/Fe islands surrounded by Co/Fe.

Before concluding this part about zero-field measurements, we want to emphasize that we observe a strong impact of Co/Fe onto the magnetic configuration within Pd/Fe. The presence of a ferromagnetic domain at the island edge, seems to impose the formation of a ferromagnetically ordered rim in Pd/Fe, which forces the spin spiral to change its propagation direction at the edge and also helps to stabilize different skyrmionic states in zero-field.

Skyrmions at the edge. Whereas we have seen that the Co/Fe rim stabilizes skyrmions in zero-field, in the following we want to study the impact of the ferromagnetic rim on field-induced skyrmions. Figure 3a shows a measurement of two differently stacked Pd/Fe islands in a perpendicular magnetic field of $B = -2$ T. Both islands are surrounded by thin patches of Co/Fe
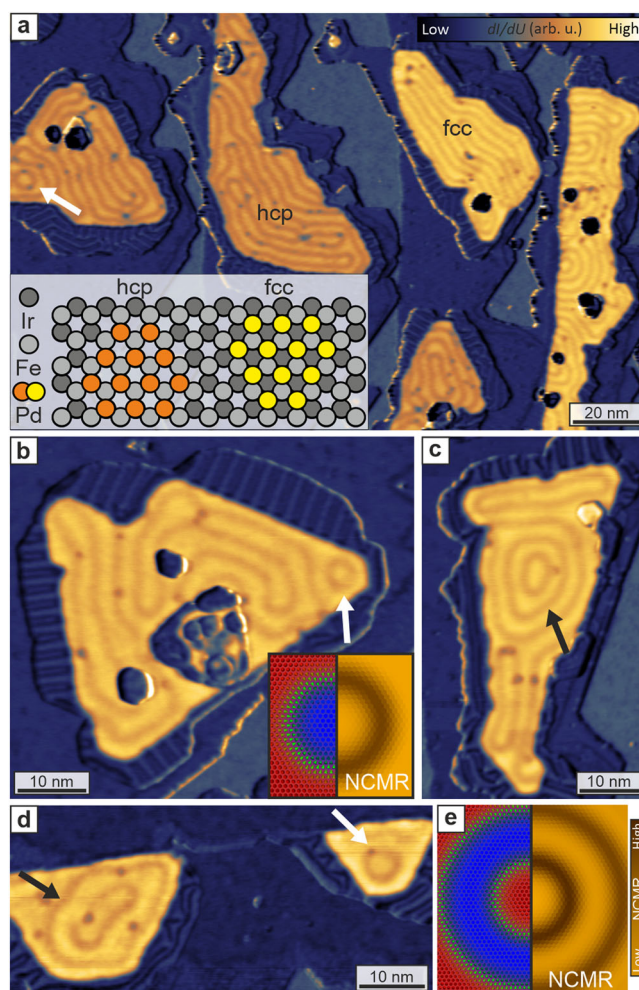

Fig. 2 Skyrmions and target states in the magnetic virgin state. a Spin spirals in hcp-stacked (orange) and fcc-stacked (yellow) Pd/Fe islands are affected by the Co/Fe rim in a similar fashion; the inset shows a sketch of the two possible stacking orders. **b** Pd/Fe island with a zero-field skyrmion (white arrow) in a corner; the inset shows the spin structure and the expected non-collinear magnetoresistance (NCMR) contrast of a skyrmion. In the spin structure red and blue areas represent opposite out-of-plane directions, in-plane oriented spins are depicted as green cones. **c** Magnetic target state (black arrow), almost fully encircled by a third ring. **d** Target state and zero-field skyrmion confined inside relatively small Pd/Fe islands. **e** Spin structure of a magnetic target state and the corresponding NCMR contrast. All differential conductance (dI/dU) maps: tunneling current $I = 3$ nA, bias voltage $U = 710$ mV.
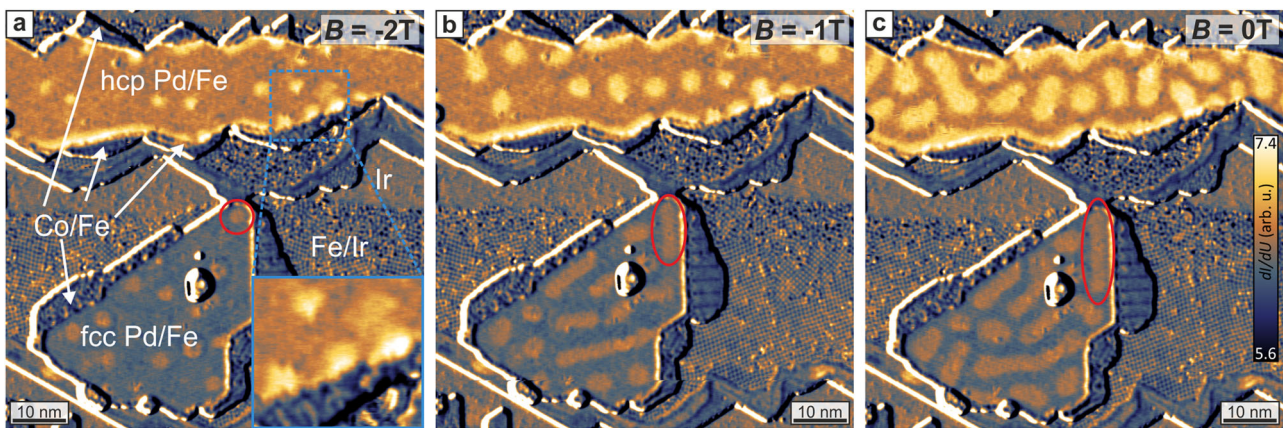
Fig. 3 Remanent skyrmions after magnetic field-sweep. a Two differently stacked Pd/Fe islands surrounded by Co/Fe in an external field $B = -2$ T; skyrmions can be written or deleted by scanning the sample surface with a sufficiently high bias voltage[6]. Inset shows a zoom-in of the magnetic objects at the island rim. **b** The same two islands after reducing the external field to $B = -1$ T. **c** Final image at $B = 0$ T; Many skyrmions have survived and are now in a metastable state. A skyrmion performing a partial strip-out parallel to the island edge is encircled in red. All differential conductance (dI/dU) maps: tunneling current $I = 3$ nA, bias voltage $U = 20$ mV.

along most parts of the island boundary. Instead of spin spirals, the Pd/Fe islands are now filled with several skyrmions in an otherwise ferromagnetic background. When the external field is reduced to -1 T in Fig. 3b and finally 0 T in Fig. 3c, the skyrmion size increases, and some skyrmions perform a partial strip-out (typically parallel to the island edge). However, even at 0 T many skyrmions survive, likely because they cannot connect to the island edge, which is the dominant pathway of skyrmion annihilation in low magnetic fields[33]. Such a stabilizing effect was also predicted for the edge tilt occurring at the boundary of magnetic materials due to DMI[37,41]. Yet, experimentally we observe that in free-standing Pd/Fe islands, skyrmions typically strip out and connect to the island rim upon a decrease of B, forming spiral stripes perpendicular to the edge (Supplementary Fig. S3). We conclude that skyrmion escape via the island edge is effectively inhibited by the adjacent ferromagnetic Co/Fe.

In both Pd/Fe islands shown in Fig. 3, the skyrmions survive in remanence at 0 T due to the modification at the island rim, yet we find significant differences in the skyrmion-edge interaction between the two Pd/Fe stacking types. In fcc Pd/Fe the magnetic texture is typically separated from the rim and the skyrmions keep a distance of at least 1–2 nm to the island boundary. In hcp Pd/Fe, on the other hand, at $B = -2$ T the rim is populated with several magnetic objects that have a similar size and shape as the skyrmions inside the island, see inset. When the field is lowered, these objects eventually become larger and form more continuous single spiral-like stripes, that seemingly prevent skyrmions from inside the island to connect to the island edge. Even in measurements using a relatively high bias voltage of $U = 710$ mV (Fig. 4), which has been shown to affect the magnetic structure and can induce skyrmion displacement, nucleation, or annihilation (red circles), the skyrmion-like objects at the Co/Fe rim remain relatively stable.

In order to investigate the origin of these different edge interactions in hcp- and fcc-stacked Pd/Fe, we will now look more closely at the structure of the Co/Fe reconstruction and how it connects to the Pd/Fe island edge. Figure 4a shows a dI/dU map of an fcc-stacked Pd/Fe island encompassed by Co/Fe and filled with several skyrmions. Figure 4b and c show a constant-current image and a dI/dU map of the same hcp-stacked Pd/Fe island surrounded by three rotational domains of the Co/Fe reconstruction, while Fig. 4d and e show a zoom-in of a Co/Fe area located between a hcp-stacked and fcc-stacked Pd/Fe island. The contrast
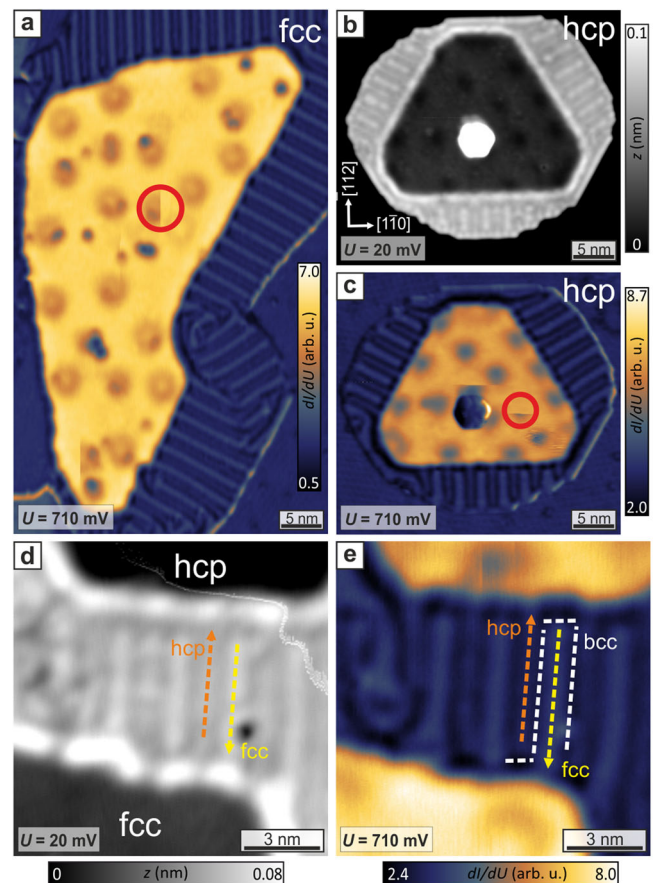

Fig. 4 Differences between fcc- an hcp-stacked Pd/Fe islands. a A differential conductance (dI/dU) map of an fcc-stacked Pd/Fe island in an applied external field. The contrast is dominated by the non-collinear magnetoresistance effect. **b** Constant-current image with apparent sample height z of a triangular hcp-stacked Pd/Fe island, surrounded by Co/Fe. **c** dI/dU map of the same island, scanned at a different bias voltage U. Red circles indicate skyrmions being written or deleted by the scanning procedure. **d** Close-up constant-current image of a Co/Fe area located between a hcp-stacked and fcc-stacked Pd/Fe island; the reconstruction pattern changes close to the island rim. **e** dI/dU map of the same area, the different hollow site sections, and the bcc(110)-like bridge sites can be clearly distinguished. All images: tunneling current $I = 3$ nA, $B = 2$ T.

on the Co/Fe reconstruction shows three distinct sections with a period of 2.5 nm, reminiscent of the uniaxial reconstruction of the Fe double layer on Ir(111)[51]. Here we have developed a similar model (Supplementary Fig. S4), in which the Co atom lattice is compressed by 10% along the close-packed [1$\bar{1}$0] direction and the Co atoms continuously shift between hcp and fcc hollow sites with bcc(110)-like bridge sections in between.

The reconstructed Co/Fe does not directly attach itself to the Pd/Fe island edge, instead, we observe a narrow transition region. This can be seen e.g., in Fig. 4b, which shows an approximately 1 nm wide bright rim surrounding the Pd/Fe island. The bias dependence of the recorded contrast (see also Supplementary Fig. S5), makes it difficult to interpret such STM data, yet we propose that the first couple of Co atomic rows at the Pd/Fe island edge grow pseudomorphic—with the same stacking as the adjacent Pd/Fe—and that only further from the edge the Co/Fe transitions into its reconstructed phase. On both sides of the Co/Fe stripe in Fig. 4d, e different sections of the reconstructed Co/Fe merge with the respective pseudomorphic Co/Fe transition region. This leads to the displayed assignment of hcp and fcc lines in the reconstructed Co/Fe. We expect that different magnetic properties of the differently stacked pseudomorphic Co/Fe areas are fundamental to understand why the skyrmion-like objects pin to the island edge or not, as observed for hcp- and fcc-stacked Pd/Fe, respectively.

Further examples of hcp-stacked Pd/Fe islands (Fig. 5a–c), show that in an applied field the island rim is actually populated with different skyrmionic objects. On the one hand, there are localized skyrmion-like states (blue arrows) that have a similar size and shape as the skyrmions in the island interior, hence we call them edge-skyrmions, on the other hand, we also find more stripped-out objects (green arrows) that resemble a single spin spiral stripe. These two types of objects typically pin to different parts of the Co/Fe rim. Through analysis of all available data, we find a general trend: in areas where the dislocation lines in the adjacent Co/Fe (see dashed lines) are perpendicular to the Pd/Fe island edge, we typically find edge-skyrmions. On the other hand,

if the dislocation lines run parallel or with an angle of up to 30° towards the rim, we dominantly find spiral stripes. Figure 5d, e schematically illustrate this trend, and also display the relation to the easy magnetization axis of Co/Fe. These findings indicate that it is possible to realize several different magnetic states at the island rim by a slight modification of the surrounding material properties.

Skyrmion-edge interactions. The findings of the previous section have inspired us to investigate the role of different magnetic interactions with regard to their ability to pin or repel skyrmions at the island edge. We employ atomistic spin dynamics simulations[52] using the following standard Hamiltonian for skyrmions in ultra-thin films[40]:

$$H = -J \sum_{\langle i,j \rangle} (\mathbf{S}_i \cdot \mathbf{S}_j) - \sum_{\langle i,j \rangle} \mathbf{D}_{i,j} \cdot (\mathbf{S}_i \times \mathbf{S}_j)$$
$$- \sum_i K_z \cdot S_{i,z}^2 - \sum_i K_x \cdot S_{i,x}^2 - \mu \sum_i (\mathbf{B} \cdot \mathbf{S}_i) \quad (1)$$

where S_i and S_j are classical spins with $|S| = 1$, J is an effective Heisenberg exchange interaction coefficient mapped on the nearest-neighbor exchange, $\mathbf{D}_{i,j}$ is the Dzyaloshinksii–Moriya vector acting on nearest-neighbor spins, K_z is the uniaxial anisotropy parameter and μ is the strength of the magnetic moment. Due to the small volume of magnetic material in our system, we expect only a minor impact by the stray-field and therefore do not include dipole-dipole interactions. The film system consisting of Pd/Fe and Co/Fe is mapped onto a single hexagonal monolayer with three different regions: a Pd/Fe area which hosts spin spirals and skyrmions, a ferromagnetic Co/Fe area with a uniaxial in-plane anisotropy K_x and lastly a narrow pseudomorphic transition region in between to represent the changes of the Co/Fe structure close to the Pd/Fe island. We use a magnetic moment of $\mu = 3\mu_B$ as calculated for Pd/Fe[53] in the entire layer and vary the magnetic interaction parameters to mimic the different materials (Table 1). For Pd/Fe, we use experimentally determined magnetic parameters[47]. The magnetic parameters of the reconstructed Co/Fe are unknown, and we chose values that reflect our experimental findings. In particular, we find that Co/Fe is nearly aligned with an out-of-plane applied magnetic field of 2 T (see "Methods" section and Supplementary Fig. S6). The pseudomorphic Co/Fe area in between Pd/Fe and reconstructed Co/Fe is represented by 4 atomic rows. Whereas experimentally it is difficult to precisely determine the width of this transition area, our simulations show that the exact number of atomic rows is not crucial for the results presented in the following. Because this Co/Fe area is not reconstructed an isotropic easy plane anisotropy of $K_z = -0.25$ meV/atom is chosen.

The simulation shown in Fig. 6a was performed at 0 K with an applied external field of $B = 2$ T. The three different areas of the lattice are indicated by dashed lines. In the initial state, a single skyrmion was written in a ferromagnetic background at the position marked by the white cross, its outer rim touching the
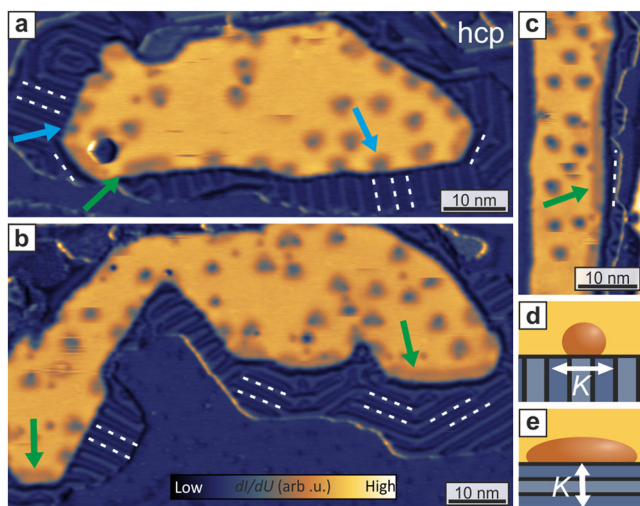

Fig. 5 Details of the skyrmion-edge interaction in hcp-stacked Pd/Fe. a–c Differential conductance (d*I*/d*U*) maps of hcp-stacked Pd/Fe islands with localized edge-skyrmions (blue arrows) and more stripped-out spiral stripes (green arrows) at the island edge. Dashed lines indicate the direction of the dislocation lines in the adjacent Co/Fe. **d, e** Simplified sketches showing the two skyrmionic objects pinned at different Co/Fe edge types and their relation to the direction of the magnetocrystalline anisotropy *K* at the rim. All d*I*/d*U* maps: tunneling current *I* = 3 nA, bias voltage *U* = 710 mV, *B* = 2 T.

Table 1 Spin dynamics simulation parameters.

Bilayer	Exchange	DMI	Anisotropy
Pd/Fe	$J = 2.86$	$D = 0.76$	$K_z = 0.4$, $K_x = 0$
Co/Fe ps (a–f)	$J = $ varied	$D = 0.76$	$K_z = -0.25$, $K_x = 0$
Co/Fe ps (i–g)	$J = 2.86$	$D = $ varied	$K_z = -0.25$, $K_x = 0$
Co/Fe re	$J = 7.86$	$D = 0.76$	$K_z = 0.4$, $K_x = 0.65$

Strength of the magnetic interaction parameters (exchange interaction J, Dzyaloshinskii–Moriya interaction D and magnetocrystalline anisotropy K) used for the spin dynamics simulation in Fig. 6 (meV/atom). The simulated layer is split into three different areas, representing the different sample bilayers found in the experiment. The skyrmion hosting Pd/Fe bilayer, the pseudomorphic (ps) Co/Fe transition area, and the reconstructed (re) Co/Fe.
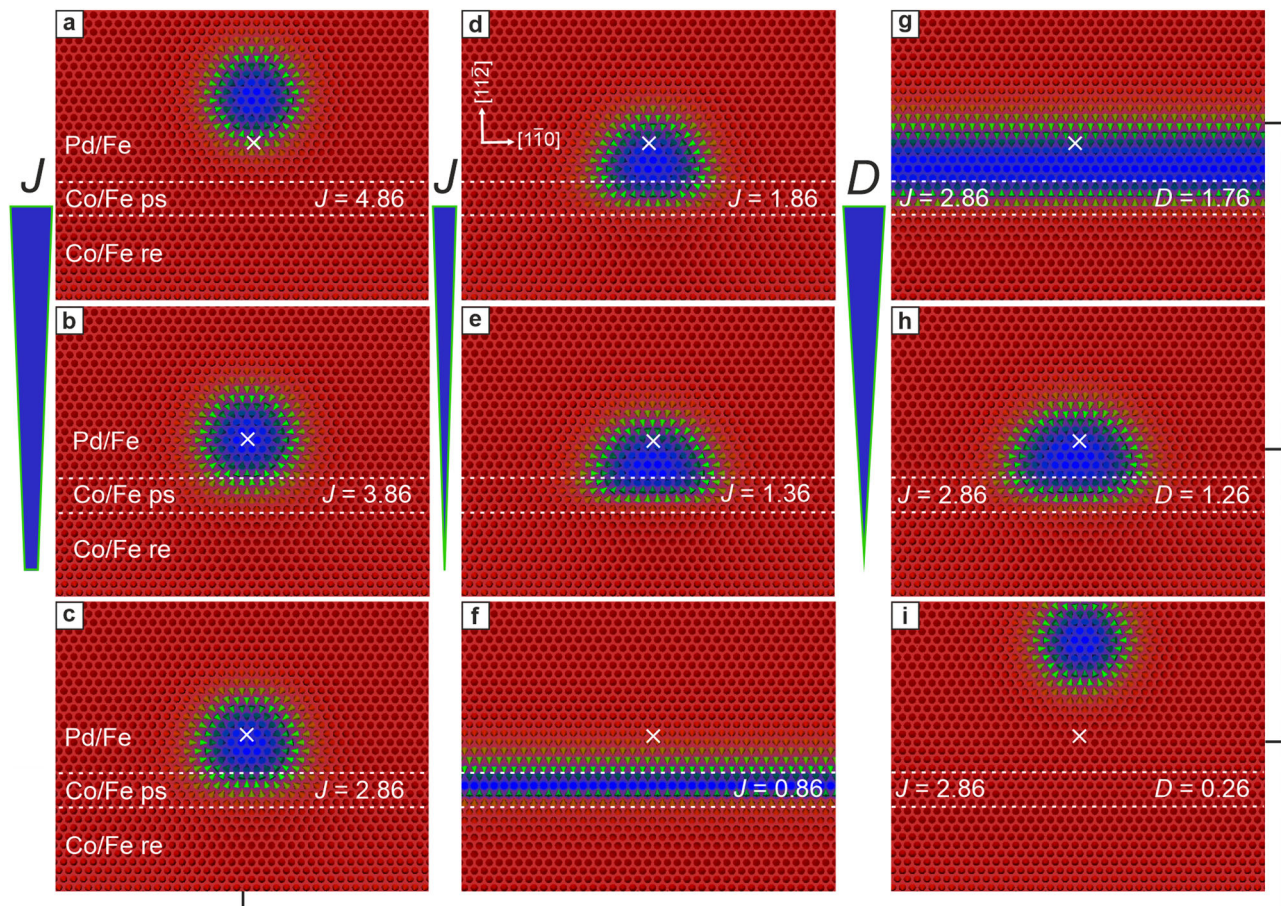
Fig. 6 Varying J and D in the pseudomorphic Co/Fe transition area. a–f Spin dynamics simulations with different values for the exchange interaction J and **g–i** the Dzyaloshinskii–Moriya interaction D in the pseudomorphic Co/Fe area. The hexagonal lattice is split in three distinct sections, as marked by the dashed lines, with different magnetic interaction parameters (Table 1) to represent the Pd/Fe bilayer and the pseudomorphic (ps) and reconstructed (re) Co/Fe bilayer. Red and blue areas represent spins pointing in opposite out-of-plane directions. In-plane pointing spins are visualized as green cones. Initially, the skyrmion was written at the position of the white cross. The displayed area was cut from a larger simulation area, see "Simulation" section of "Methods". All simulations were performed at $T = 0$ K and $B = 2$ T.
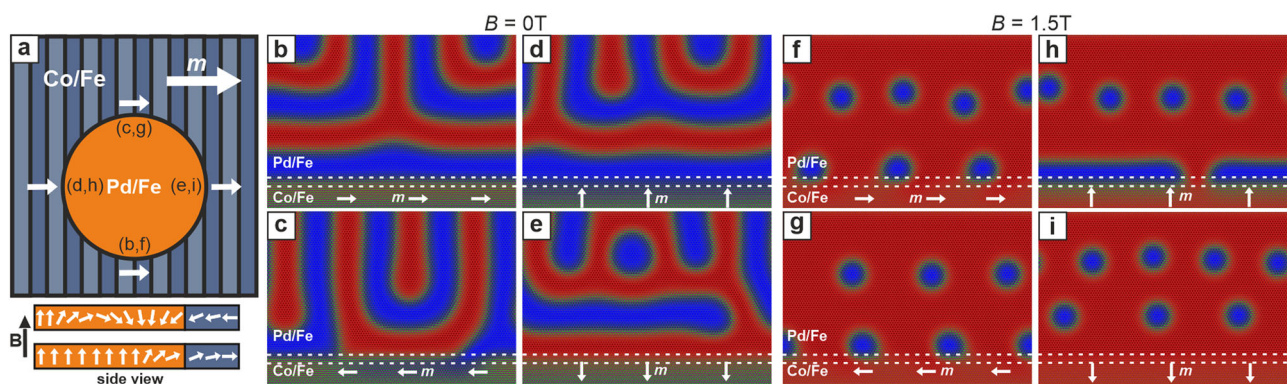

Fig. 7 Rotating the in-plane magnetization component in the reconstructed Co/Fe. a Schematic overview of the four magnetization directions and side view of a clockwise spin rotation at the edge with and without incorporating an edge-skyrmion. **b–e** Simulations at zero magnetic field and **f–i** at $B = 1.5$ T. The hexagonal lattice has periodic boundary conditions in the horizontal direction and is split into three distinct areas with the magnetic parameters as shown in Table 1 with exchange interaction $J = 2.86$ meV/atom and Dzyaloshinskii–Moriya interaction $D = 0.76$ meV/atom in the pseudomorphic transition area. The white arrows indicate the in-plane magnetization component m of the reconstructed Co/Fe. Red and blue areas represent spins pointing in opposite out-of-plane directions, while in-plane pointing spins are green.

pseudomorphic Co/Fe area. During the simulation, the skyrmion was repelled from the Co/Fe edge and slowly moved further inside the Pd/Fe film. To now investigate the role of magnetic interactions at the Pd/Fe edge, we vary the strength of different

parameters in the pseudomorphic Co/Fe area. First, the strength of the exchange interaction is reduced step-wise from 4.86 meV/atom to 0.86 meV/atom in Fig. 6a–f, while DMI is kept constant at the same value as the adjacent Pd/Fe. When J is considerably

higher in the pseudomorphic Co/Fe area than in Pd/Fe (Fig. 6a), the skyrmion is repelled from the boundary during the simulations. In Fig. 6c, exchange and DMI have the same strength in the transition area as in Pd/Fe. Here the skyrmion is pinned to the edge only by the in-plane anisotropy, which is energetically more favorable for the outer skyrmion part than the out-of-plane anisotropy within Pd/Fe. With a smaller J (Fig. 6d, e), the skyrmion moves further inside the pseudomorphic Co/Fe area, because here a large nearest-neighbor spin angle does not cost as much exchange energy, compared to the Pd/Fe area. The reconstructed Co/Fe area with its relatively high exchange interaction on the other hand serves as a barrier and prevents the skyrmion from entering the Co/Fe completely. Finally, when J is sufficiently small the skyrmion strips out along the edge and is fully confined within the Co/Fe transition area (Fig. 6f).

We repeat such simulations but now vary the strength of the DMI vector $D = |\mathbf{D}_{i,j}|$ (Fig. 6g–i), the exchange interaction is set to the same values as in Pd/Fe ($J = 2.86$ mV/atom). Here the skyrmion is repelled when D becomes very small and strips out into a single spin spiral stripe for a larger D. We find that there is a certain parameter range for both J and D in which the skyrmion is stable at the edge (Supplementary Fig. S7). When the skyrmions pin to the Co/Fe edge, their spin structure continues inside the Co/Fe transition region, and their topological charge is preserved. Based on these simulations we conclude that the magnetic objects at the Pd/Fe island edge are indeed skyrmions. We also observe that already small parameter changes in the Co/Fe transition area can be the cause for skyrmion pinning at the edge of hcp-stacked Pd/Fe but not at the edge of fcc-stacked Pd/Fe. Furthermore, we find that for the edge-pinning two distinct areas are needed, that together exhibit a Lennard–Jones-like potential: a narrow area that is favorable for certain parts of the skyrmion structure, and also a repulsive area, that prevents the skyrmions from fully leaving the Pd/Fe island.

The reconstructed Co/Fe of Fig. 6 was nearly saturated by the applied magnetic field of $B = 2$ T, making it effectively an out-of-plane magnetized surrounding. We now turn to simulations with smaller magnetic fields, where the in-plane magnetization component m of Co/Fe is larger, and investigate its effect on the magnetic state of Pd/Fe near the boundary. In Fig. 7, simulations were performed both in zero field and with field-cooling at $B = 1.5$ T from a random configuration at 80 K down to 0 K (see "Methods" section). To induce different magnetization directions at the boundary of the reconstructed Co/Fe, as observed experimentally, the relative in-plane anisotropy axis K_x was changed as indicated by the white arrows (Fig. 7a). The magnetization of the lowest Co/Fe atomic row was fixed in the same direction, while all other spins were able to relax freely. Figure 7b–e shows the simulations at $B = 0$ T, which arrive at very similar spin spiral structures as we have observed them experimentally in the magnetic virgin state (cf. Fig. 2), with spin spiral stripes parallel to the boundary and occasional zero-field skyrmions. When the magnetization in Co/Fe points parallel to the boundary (Fig. 7b, c), the spin spiral stripes are dominantly parallel to the edge, and the phase of the spiral, i.e., whether the spiral spins are pointing up (red) or down (blue), does not seem to make a difference. When the magnetization is perpendicular to the edge (Fig. 7d, e), the spiral phase clearly depends on the magnetization direction of the Co/Fe area, which can be attributed to the presence of DMI preferring clockwise rotational sense. We also observe the spontaneous formation of a zero-field skyrmion in Fig. 7e.

At $B = 1.5$ T the magnetization of the reconstructed Co/Fe area has begun to rotate towards the out-of-plane direction. Yet an in-plane component remains and we can still find differences between different in-plane directions: when the magnetization is

parallel to the boundary (Fig. 7f, g), circular skyrmions appear spontaneously at the edge and remain stable during the simulation process. With the magnetization pointing perpendicular to the edge (Fig. 7h, i), we observe the following: first, in Fig. 7h, a stripped-out skyrmion similar to a single spin spiral stripe is stabilized at the edge. Secondly, for the opposite magnetization direction neither compact nor stripped-out skyrmions are stable at the edge, as shown in Fig. 7i. Here the incorporation of skyrmions at the edge would require an anticlockwise spin rotation towards the edge, which is unfavorable for the DMI in this system. However, in Fig. 7h a clockwise rotation only becomes possible through the inclusion of an edge-skyrmion, see side view sketch in Fig. 7a. Therefore, skyrmions are repelled in Fig. 7i but not in Fig. 7h.

Discussion

Our work demonstrates that by altering the edge properties of a film its magnetic state can be effectively manipulated. Here the ferromagnetic Co/Fe rim changes the propagation direction of the spin spiral in Pd/Fe so that the spiral stripes are parallel to the island edge instead of perpendicular. As shown in the simulations, the in-plane magnetization direction of the rim can also have a small effect on how the spiral connects to the boundary. Furthermore, depending on the size and shape of the Pd/Fe island, the Co/Fe rim enables the formation of zero-field skyrmions and target states in the magnetic virgin state. Judging by the unique spin spiral structures we find in the magnetic virgin state of our system, one might also be able to utilize the edge to stabilize a zoo of different topological spin states like, e.g., the recently discussed skyrmion bags[54,55].

The Co/Fe rim increases the amount of skyrmions that survive in the remanent state. In fcc-stacked Pd/Fe this happens, because a connection between skyrmions and the boundary is hindered by the ferromagnetic surroundings. In hcp-stacked Pd/Fe the edge-pinned skyrmions strip out along the Co/Fe rim when the field is lowered and hinder further skyrmions from connecting to the edge by repulsive skyrmion–skyrmion interactions. In both cases, we anticipate that these additional repulsive forces at the boundary would counteract the SkHE and effectively prevent skyrmion annihilation. Our spin dynamics simulations have shown that there are several material parameters that can be responsible for a repulsion or pinning of skyrmions at the film edge, e.g., the edge-pinning observed in hcp Pd/Fe can be caused by either lower exchange interactions, higher DMI, or stronger easy plane anisotropy at the island rim.

Furthermore, we have observed in experiments and simulations that the magnetization direction at the Co/Fe boundary has an effect on the edge-skyrmions in hcp Pd/Fe. A magnetization parallel to the edge favors the formation of localized skyrmions, while a perpendicular magnetization enables the skyrmions to strip out along the edge even in applied external fields. While we use a self-organized model system to investigate skyrmion physics, we anticipate that these findings can also be applied to top-down approaches to deliberately create structures with different magnetic properties, as it has been shown to be viable by Ohara et al.[27] and Juge et al.[44]. Modifying the boundaries of a skyrmion system with tailored materials is a means to set up guard railings, which can improve the speed and reliability of potential skyrmion devices.

Finally, we want to propose a possible application for edge-pinned skyrmions: in skyrmion racetrack memory devices the information is stored in the distance between skyrmions[13]. Therefore such devices must rely on equidistant bit positions. Yet there are several factors that can change the distances between skyrmions including thermal drift, noise generated by device
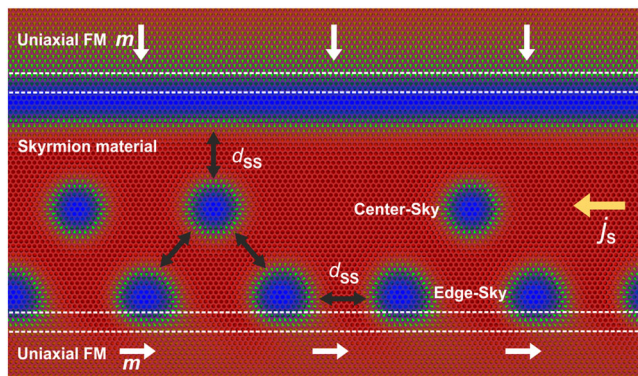
Fig. 8 Racetrack with edge-skyrmions. Possible racetrack structure with edge-skyrmions functioning as spacers between skyrmion bits. The material parameters are the same as shown in Table 1 with exchange interaction $J = 2.86$ meV/atom and Dzyaloshinskii–Moriya interaction $D = 0.76$ meV/atom in the transition area. At the upper rim, the in-plane magnetization component m of the ferromagnetic (FM) Co/Fe is orthogonal to induce a skyrmion-repelling spiral stripe. Center- and edge-skyrmions are moved simultaneously by a spin-polarized current j_s. The minimum distance between two skyrmions d_{SS} is determined by repulsive skyrmion-skyrmion interactions. Red and blue areas represent spins pointing in opposite out-of-plane directions, while in-plane pointing spins are green. $B = 1.5$ T and $T = 0$ K.

operation, as well as attractive or repulsive skyrmion-skyrmion interactions. To overcome these challenges different approaches have been put forward, e.g., the use of a two-lane racetrack[56], or a periodic arrangement of notches[57]. We propose the use of edge-skyrmions as spacers to divide the track into separated skyrmion-sized bits as shown in Fig. 8. In the displayed setup the skyrmion track is confined between two ferromagnetic Co/Fe edges, one with perpendicular and the other with parallel magnetization at the edge. The information is contained in the central row, stored in the absence or presence of a skyrmion along the track. The upper Co/Fe rim repels skyrmions—here realized by inducing a single spin spiral stripe—and forces skyrmions in the center of the track to interact with the edge-skyrmions at the bottom rim. The minimum distance between skyrmions d_{SS} leaves enough space for one center-skyrmion to be positioned between two edge-skyrmions and the upper rim. Additionally, the repulsive inter-actions with edge-skyrmions hinder center-skyrmions from hopping from one bit to another. It is anticipated that all sky-rmions, the ones that store the information and the ones that are used as bit separators, move coherently under lateral currents. Additionally, small distance variations between bits could be corrected, because each arrival of an edge-skyrmion near the read/write unit would unambiguously signal the beginning of a new bit.

Methods

Experimental details. The samples were prepared and investigated in an ultra-high vacuum system with different chambers for crystal cleaning, metal deposition, and STM measurements. The Ir(111) crystal surface was cleaned by cycles of annealing in an oxygen atmosphere of 10^{-6}–10^{-8} mbar while slowly ramping the crystal temperature to about $T = 1600$ K and subsequent sputtering with Ar-ions. The surface was cured by a final 60 s long electron-beam flash to 1600 K. Approximately 0.7 atomic layers of Fe were deposited onto the crystal, while the crystal temperature was still elevated (≈400 K), followed by 0.5 atomic layers of Pd and finally 0.2 atomic layers of Co. The Co was deposited 30 min after the electron-beam flash with the sample now being closer to room temperature.

Our home-built STM is equipped with a superconducting magnet, that can generate magnetic fields of up to 9 T perpendicular to the sample surface. All STM measurements were performed at 4 K. I is the tunneling current and U is the bias set between tip and sample. The dI/dU maps are recorded simultaneously with the constant-current topographies using the lock-in technique. We use a Cr bulk tip which can have an arbitrary magnetization axis and varying degrees of spin-polarization[58]. In SP-STM, the spin-polarized tunneling current depends on the cosine of the angle between tip and sample magnetization. By gentle contact with the sample, the magnetization axis of the Cr tip can be altered. In this way, Cr tips can be used to probe both in-plane and out-of-plane components of the sample magnetization.

Simulations. For the magnetic parameters of the reconstructed Co/Fe area, we chose to increase the strength of the exchange interaction with respect to Pd/Fe while keeping the DMI contribution at the same value. As an interfacial effect, we anticipate the DMI to mainly act on the Fe layer while the exchange interaction contributes to both layers of Co/Fe. The Co/Fe bilayer exhibits in-plane ferro-magnetic domains, magnetized perpendicular to the dislocation lines. We simulate this by adding an in-plane uniaxial anisotropy energy parameter $K_x = 0.65$ meV/atom. Furthermore, as shown in Supplementary Fig. S6, in a perpendicular field of $B = 2$ T the Co/Fe magnetization axis has a large out-of-plane component. We assume that the Co/Fe is more easily magnetized compared to Pd/Fe because its total magnetic moment is larger. However, due to software limitations, we cannot increase the magnetic moment of Co/Fe separately, therefore we instead include an additional out-of-plane anisotropy parameter K_z for the reconstructed Co/Fe and adjust the strength of both anisotropy parameters to reflect our experimental findings and finally arrive at the parameter set shown in Table 1.

Atomistic spin dynamics simulations were performed using the MonteCrystal simulation code which can be found on github[52]. The code employs an algorithm that numerically solves the Landau–Lifshitz–Gilbert equation. For all simulations, the damping parameter was set to $\alpha = 0.5$. The simulated lattice consisted of 80 rows with 100 atomic sites each and periodic boundary conditions in the horizontal direction. The reconstructed Co/Fe was modeled with 10 atomic rows, while the pseudomorphic Co/Fe was 4 atom rows thick. The simulations of Fig. 6 were carried out for at least 250 ps and were stopped either after they had converged with the skyrmion pinned at the edge or after the skyrmion was repelled. The simulations of Fig. 7 were started from a random spin configuration and the temperature was reduced in 2 K steps from 80 to 0 K until the energy reached a stable value.

Data availability
The data that support the findings of this study are available from the authors upon reasonable request.

Code availability
The spin dynamics simulations of the manuscript were done with MonteCrystal 3.2.0, which can be found on github[52].

References
1. Bogdanov, A. N. & Yablonskii, D. A. Thermodynamically stable "vortices" in magnetically ordered crystals. The mixed state of magnets. *Sov. Phys. JETP* **68**, 101–103 (1989).
2. Bogdanov, A. N. & Hubert, A. Thermodynamically stable magnetic vortex states in magnetic crystals. *J. Magn. Magn. Mater.* **138**, 255–269 (1994).
3. Mühlbauer, S. et al. Skyrmion lattice in a chiral magnet. *Science* **323**, 915–919 (2009).
4. Yu, X. Z. et al. Real-space observation of a two-dimensional skyrmion crystal. *Nature* **465**, 901–904 (2010).
5. Heinze, S. et al. Spontaneous atomic-scale magnetic skyrmion lattice in two dimensions. *Nat. Phys.* **7**, 713–718 (2011).
6. Romming, N. et al. Writing and deleting single magnetic skyrmions. *Science* **341**, 636–639 (2013).
7. Sampaio, J., Cros, V., Rohart, S., Thiaville, A. & Fert, A. Nucleation, stability and current-induced motion of isolated magnetic skyrmions in nanostructures. *Nat. Nanotechnol.* **8**, 839 (2013).
8. Nagaosa, N. & Tokura, Y. Topological properties and dynamics of magnetic skyrmions. *Nat. Nanotechnol.* **8**, 899–911 (2013).
9. Kang, W., Huang, Y., Zhang, X., Zhou, Y. & Zhao, W. Skyrmion-electronics: an overview and outlook. *Proc. IEEE* **104**, 2040–2061 (2016).
10. Everschor-Sitte, K., Masell, J., Reeve, R. M. & Kläui, M. Perspective: magnetic skyrmions–overview of recent progress in an active research field. *J. Appl. Phys.* **124**, 240901 (2018).
11. Zhang, X. et al. Skyrmion-electronics: writing, deleting, reading and processing magnetic skyrmions toward spintronic applications. *J. Phys. Condens. Matter* **32**, 143001 (2020).

12. Parkin, S. S., Hayashi, M. & Thomas, L. Magnetic domain-wall racetrack memory. *Science* **320**, 190–194 (2008).

13. Fert, A., Cros, V. & Sampaio, J. Skyrmions on the track. *Nat. Nanotechnol.* **8**, 152–156 (2013).

14. Zhang, X., Ezawa, M. & Zhou, Y. Magnetic skyrmion logic gates: conversion, duplication and merging of skyrmions. *Sci. Rep.* **5**, 9400 (2015).

15. Luo, S. et al. Reconfigurable skyrmion logic gates. *Nano Lett.* **18**, 1180–1184 (2018).

16. Song, M. et al. Logic device based on skyrmion annihilation. *IEEE Trans. Electron Devices* **68**, 1939–1943 (2021).

17. Pinna, D. et al. Skyrmion gas manipulation for probabilistic computing. *Phys. Rev. Appl.* **9**, 064018 (2018).

18. Zázvorka, J. et al. Thermal skyrmion diffusion used in a reshuffler device. *Nat. Nanotechnol.* **14**, 658–661 (2019).

19. Jibiki, Y. et al. Skyrmion brownian circuit implemented in continuous ferromagnetic thin film. *Appl. Phys. Lett.* **117**, 082402 (2020).

20. Dzyaloshinskii, I. Thermodynamic theory of weak ferromagnetism in antiferromagnetic substances. *Sov. Phys. JETP* **5**, 1259–1272 (1957).

21. Moriya, T. Anisotropic superexchange interaction and weak ferromagnetism. *Phys. Rev.* **120**, 91–98 (1960).

22. Hsu, P.-J. et al. Electric-field-driven switching of individual magnetic skyrmions. *Nat. Nanotechnol.* **12**, 123 (2017).

23. Meyer, S. et al. Isolated zero field sub-10 nm skyrmions in ultrathin Co films. *Nat. Commun.* **10**, 3823 (2019).

24. Jiang, W. et al. Blowing magnetic skyrmion bubbles. *Science* **349**, 283–286 (2015).

25. Woo, S. et al. Observation of room-temperature magnetic skyrmions and their current-driven dynamics in ultrathin metallic ferromagnets. *Nat. Mat.* **15**, 501–506 (2016).

26. Soumyanarayanan, A. et al. Tunable room-temperature magnetic skyrmions in Ir/Fe/Co/Pt multilayers. *Nat. Mat.* **16**, 898–904 (2017).

27. Ohara, K. et al. Confinement and protection of skyrmions by patterns of modified magnetic properties. *Nano Lett.* **21**, 4320–4326 (2021).

28. Schulz, T. et al. Emergent electrodynamics of skyrmions in a chiral magnet. *Nat. Phys.* **8**, 301–304 (2012).

29. Jiang, W. et al. Direct observation of the skyrmion Hall effect. *Nat. Phys.* **13**, 162–169 (2017).

30. Litzius, K. et al. Skyrmion Hall effect revealed by direct time-resolved x-ray microscopy. *Nat. Phys.* **13**, 170–175 (2017).

31. Iwasaki, J., Mochizuki, M. & Nagaosa, N. Current-induced skyrmion dynamics in constricted geometries. *Nat. Nanotechnol.* **8**, 742–747 (2013).

32. Purnama, I., Gan, W. L., Wong, D. W. & Lew, W. S. Guided current-induced skyrmion motion in 1D potential well. *Sci. Rep.* **5**, 10620 (2015).

33. Bessarab, P. F. et al. Lifetime of racetrack skyrmions. *Sci. Rep.* **8**, 3433 (2018).

34. Barker, J. & Tretiakov, O. A. Static and dynamical properties of antiferromagnetic skyrmions in the presence of applied current and temperature. *Phys. Rev. Lett.* **116**, 147203 (2016).

35. Zhang, X., Zhou, Y. & Ezawa, M. Magnetic bilayer-skyrmions without skyrmion Hall effect. *Nat. Commun.* **7**, 10293 (2016).

36. Dohi, T., DuttaGupta, S., Fukami, S. & Ohno, H. Formation and current-induced motion of synthetic antiferromagnetic skyrmion bubbles. *Nat. Commun.* **10**, 5153 (2019).

37. Rohart, S. & Thiaville, A. Skyrmion confinement in ultrathin film nanostructures in the presence of Dzyaloshinskii-Moriya interaction. *Phys. Rev. B* **88**, 184422 (2013).

38. Zheng, F. et al. Direct imaging of a zero-field target skyrmion and its polarity switch in a chiral magnetic nanodisk. *Phys. Rev. Lett.* **119**, 197205 (2017).

39. Kolesnikov, A. G., Stebliy, M. E., Samardak, A. S. & Ognev, A. V. Skyrmionium – high velocity without the skyrmion Hall effect. *Sci. Rep.* **8**, 16966 (2018).

40. Hagemeister, J., Siemens, A., Rózsa, L., Vedmedenko, E. Y. & Wiesendanger, R. Controlled creation and stability of $k\pi$ skyrmions on a discrete lattice. *Phys. Rev. B* **97**, 174436 (2018).

41. Cortés-Ortuño, D. et al. Nanoscale magnetic skyrmions and target states in confined geometries. *Phys. Rev. B* **99**, 214408 (2019).

42. Lai, P. et al. An improved racetrack structure for transporting a skyrmion. *Sci. Rep.* **7**, 45330 (2017).

43. Toscano, D. et al. Suppression of the skyrmion Hall effect in planar nanomagnets by the magnetic properties engineering: Skyrmion transport on nanotracks with magnetic strips. *J. Magn. Magn. Mater.* **504**, 166655 (2020).

44. Juge, R. et al. Helium ions put magnetic skyrmions on the track. *Nano Lett.* **21**, 2989–2996 (2021).

45. Bode, M. Spin-polarized scanning tunnelling microscopy. *Rep. Prog. Phys.* **66**, 523–582 (2003).

46. Wiesendanger, R. Spin mapping at the nanoscale and atomic scale. *Rev. Mod. Phys.* **81**, 1495–1550 (2009).

47. Romming, N., Kubetzka, A., Hanneken, C., von Bergmann, K. & Wiesendanger, R. Field-dependent size and shape of single magnetic skyrmions. *Phys. Rev. Lett.* **114**, 177203 (2015).

48. Schmidt, L. et al. Symmetry breaking in spin spirals and skyrmions by in-plane and canted magnetic fields. *N. J. Phys.* **18**, 075007 (2016).

49. Hagemeister, J. C. *Confinement Effects and Stability of Spin-Spirals and Skyrmions in Ultrathin Magnetic Films* (University of Hamburg, Hamburg, 2016).

50. Hanneken, C. et al. Electrical detection of magnetic skyrmions by tunnelling non-collinear magnetoresistance. *Nat. Nanotechnol.* **10**, 1039–1042 (2015).

51. Hsu, P.-J. et al. Guiding spin spirals by local uniaxial strain relief. *Phys. Rev. Lett.* **116**, 017201 (2016).

52. Hagemeister, J. C. MonteCrysal 3.2.0, https://github.com/jhagemeister/montecrystal (2020).

53. Dupé, B., Hoffmann, M., Paillard, C. & Heinze, S. Tailoring magnetic skyrmions in ultra-thin transition metal films. *Nat. Commun.* **5**, 4030 (2014).

54. Foster, D. et al. Two-dimensional skyrmion bags in liquid crystals and ferromagnets. *Nat. Phys.* **15**, 655–659 (2019).

55. Rybakov, F. N. & Kiselev, N. S. Chiral magnetic skyrmions with arbitrary topological charge. *Phys. Rev. B* **99**, 064437 (2019).

56. Müller, J. Magnetic skyrmions on a two-lane racetrack. *N. J. Phys.* **19**, 025002 (2017).

57. Fook, H. T., Gan, W. L. & Lew, W. S. Gateable skyrmion transport via field-induced potential barrier modulation. *Sci. Rep.* **6**, 21099 (2016).

58. Schlenhoff, A., Krause, S., Herzog, G. & Wiesendanger, R. Bulk Cr tips with full spatial magnetic sensitivity for spin-polarized scanning tunneling microscopy. *Appl. Phys. Lett.* **97**, 083104 (2010).

Author contributions

J.S. performed the experiments, J.S. and A.K. prepared the samples. J.S. did the spin dynamics simulations. J.S. wrote the manuscript. J.S., E.Y.V., R.W., A.K., and K.v.B. discussed the results and contributed to the manuscript.

Competing interests

The authors declare no competing interests.

Additional information

Supplementary information The online version contains supplementary material available at https://doi.org/10.1038/s42005-021-00796-w.

Correspondence and requests for materials should be addressed to Jonas Spethmann.

Peer review information *Communications Physics* thanks Juliano Denardin and Xiaoxi Liu for their contribution to the peer review of this work. Peer reviewer reports are available.